2023 EAGE ANNUAL
84TH CONFERENCE & EXHIBITION
VIENNA | AUSTRIA

Visco-elastic full-waveform inversion and imaging using ocean-bottom node data

N. Masmoudi[1], W. Stone[1], A. Ratcliffe[1]

[1] CGG

Summary

Full-waveform inversion (FWI) has demonstrated tremendous potential to provide high-resolution models of the subsurface in different geological settings. However, in complex environments such as salt and subsalt, relying on acoustic approximations in FWI limits the accuracy of Earth models derived from modern field data, and may require complex workflows to mitigate the challenges associated with large elastic parameter variations. Recent case studies highlight this issue and suggest that more accurate models can be produced by elastic FWI using simpler workflows in these areas. In addition to elasticity, wave propagation in the subsurface undergoes anelastic (viscous) effects, especially through absorption in gas-charged layers. Although anelastic effects are known to be significant in many visco-acoustic case studies, few examples consider both elastic and anelastic effects in FWI. In this paper, we present a visco-elastic FWI to invert for P-wave velocity and associated viscosity. We demonstrate our approach using ocean-bottom node data from the Central North Sea in a complex area associated with strong velocity contrasts and shallow absorption anomalies. Results in this area demonstrate that visco-elastic FWI can provide high-resolution viscosity and velocity models, and an FWI Image with improved event continuity, resolution, and signal-to-noise ratio compared to visco-acoustic FWI.

Visco-elastic full-waveform inversion and imaging using ocean-bottom node data

Introduction

Full-waveform inversion (FWI) is designed to recover different subsurface parameters by minimising a cost function based on modelled and recorded seismic data. It is well-known that acoustic FWI can struggle in complex areas with large elastic parameter variations such as the edges of salt bodies, hard water-bottoms, basalt and chalk layers. Wavefield propagation around these structures experiences elastic effects which can impact the phase and amplitude of the modelled data. Recent case studies have highlighted the potential benefits of elastic FWI in areas of strong elasticity (for example, Plessix and Krupovnickas, 2021; Wang et al., 2021; Masmoudi et al., 2022; Wu et al., 2022). In addition to elastic phenomena, anelastic (viscous) effects (for example, from gas trapped in the shallow overburden), characterised by the quality factor Q, can distort the phase and attenuate the amplitude of the data. This can be handled in the inversion process, and several authors have shown the benefits of inverting for strong localised absorption (for example, Stopin et al., 2016; Xiao et al., 2018). Most of these FWI applications have used a visco-acoustic formulation, which works well in sedimentary layers away from large elastic parameter variations. However, several visco-elastic developments have been proposed (for example, Yang et al., 2016; Fabien-Ouellet et al., 2017). In this abstract, we present a visco-elastic FWI to invert for the P-wave velocity and associated quality factor. We show results of this approach from a Central North Sea ocean-bottom node (OBN) dataset in an area containing strong velocity contrasts and absorption related to shallow accumulations of gas. In addition, results are presented in terms of the FWI Image (Zhang et al., 2020) obtained from a 40 Hz visco-elastic FWI of the data.

Method

We formulate the visco-elastic FWI methodology in the time domain based on the generalised standard linear solid model as described in Carcione et al. (1988) and Robertson et al. (1994). The forward modelling results in the coupled first-order velocity-stress equations:

$$\begin{aligned} &\rho \partial_t \boldsymbol{v} = D\boldsymbol{\sigma}\,, \\ &\partial_t \boldsymbol{\sigma} = CD^T\boldsymbol{v} + \textstyle\sum_{l=1}^{L} \boldsymbol{r}_l\,, \\ &\partial_t \boldsymbol{r}_l = \tilde{C}D^T\boldsymbol{v} + \boldsymbol{r}_l\,, \end{aligned} \tag{1}$$

where in the 3D $(\mathrm{x}, \mathrm{y}, z)$ coordinates $\boldsymbol{v}$ is the particle velocity vector $(v_{\mathrm{x}}, v_{\mathrm{y}}, v_{\mathrm{z}})^T$, $\boldsymbol{\sigma}$ is the stress vector $(\sigma_{\mathrm{xx}}, \sigma_{\mathrm{yy}}, \sigma_{\mathrm{zz}}, \sigma_{\mathrm{xz}}, \sigma_{\mathrm{yz}}, \sigma_{\mathrm{xy}})^T$, $\boldsymbol{r}_l$ is the memory variable vector corresponding to the l^{th} mechanism defined as $\boldsymbol{r}_l = (r^l_{xx}, r^l_{yy}, r^l_{zz}, r^l_{xz}, r^l_{yz}, r^l_{xy})^T$, ρ is the density, and D is the derivative matrix given by:

$$D = \begin{pmatrix} \partial_{\mathrm{x}} & 0 & 0 & \partial_{\mathrm{z}} & 0 & \partial_{\mathrm{y}} \\ 0 & \partial_{\mathrm{y}} & 0 & 0 & \partial_{\mathrm{z}} & \partial_{\mathrm{x}} \\ 0 & 0 & \partial_{\mathrm{z}} & \partial_{\mathrm{x}} & \partial_{\mathrm{y}} & 0 \end{pmatrix}. \tag{2}$$

C and $\tilde{C}$ are stiffness matrices (using Voigt notation) describing the elastic and anelastic behaviour (Robertson et al., 1994). Further, the $\tilde{C}$ stiffness matrix is parameterised by the so-called relaxation times with their values optimised to achieve the desired constant P and S-wave quality factor (Q_P, Q_S) behaviour over a given frequency band (Blanch et al., 1995).

Our elastic scheme is a joint P-wave velocity and quality factor (V_P, Q_P) inversion. The adjoint state formulation is used to compute the FWI gradients. The S-wave velocity and associated quality factor (V_S, Q_S) are updated to maintain predefined spatially variable V_P/V_S and Q_P/Q_S ratios. The density is updated following Gardner's law. These practical assumptions allow us to reduce the number of inversion parameters, and focus on those that can be constrained from the data (i.e., V_P and Q_P). Note that these assumptions are more appropriate for an inversion driven by hydrophone recordings, while the S-wave velocity and quality factor (V_S, Q_S) are better constrained from geophone recordings which are naturally richer in shear wave information (for example, Fabien-Ouellet et al., 2017). Despite this reduction in the number of parameters, inverting for velocity and quality factor remains a well-known challenge for multi-parameter FWI of surface seismic data. Nevertheless, absorption and velocity effects have relative frequency variation (Malinowski et al., 2011) and inverting for strong absorption anomalies using a broad range of frequencies helps discriminate between V_P and Q_P.

Results

We applied our visco-elastic FWI to an approximately 100 km^2 area of a Central North Sea OBN dataset (Refaat et al., 2021). This area is known to contain shallow absorption bodies, and complex salt and sub-salt structures. Starting from a smoothed velocity model derived from an acoustic FWI workflow with tomography (Figure 1a), we updated jointly V_P and Q_P using our visco-elastic FWI and, also, equivalently with a visco-acoustic FWI (Xiao et al., 2018). Both inversions were run from 1.5 Hz to 15 Hz using hydrophone data, updating the model down to 7 km depth. The V_P perturbations from acoustic and elastic FWI (Figures 1b and 1c) are structurally similar in the sediment layers (black dashed rectangle), with the elastic perturbation showing slightly higher resolution. However, perturbations are different around the salt bodies (black arrows), chalk layer (yellow arrow) and subsalt area (green arrow). The negative/positive conformable perturbations around the top salt structures in the elastic FWI results are due to smoothing of the starting model. Meanwhile, the uniformity of the deeper subsalt perturbations can be related to better amplitude handling in the elastic case. Conversely, the V_P perturbation around and inside the salt diapir in acoustic FWI shows non-conformable character and the deeper perturbations are weaker. The acoustic FWI has performed well in the shallow sediments but has suffered from inversion artefacts around and beneath areas of strong elastic contrast. Mitigation of these issues with acoustic FWI requires complex inversion workflows and cost functions (for example, Refaat et al., 2021). For the Q_P model, starting from a constant model (Figure 1d), both acoustic and elastic FWI have produced similar shallow absorbing bodies as shown in Figures 1e and 1f, respectively, with the elastically derived model showing slightly higher resolution. The dotted black line in the inline and depth sections shows the strongest absorption is located on top of the salt diapir. Inverting for such localised anomalies was important to obtain an accurate V_P update in the shallow and deeper sections.

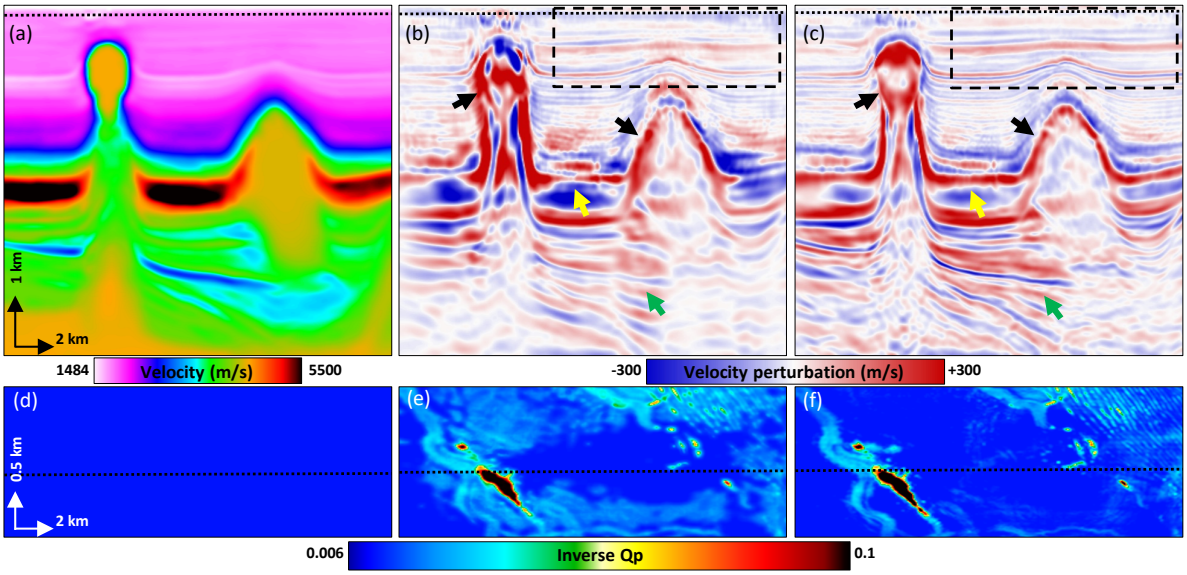

Figure 1 *Inline sections of visco-acoustic and visco-elastic joint V_P and Q_P FWI: (a) starting V_P, (b) 15 Hz V_P perturbation after visco-acoustic joint FWI, and (c) 15 Hz V_P perturbation after visco-elastic joint FWI. Depth slices at 270 m of: (d) starting $1/Q_P$ model, (e) 15 Hz $1/Q_P$ model after visco-acoustic joint FWI, and (f) 15 Hz $1/Q_P$ model after visco-elastic joint FWI.*

Single parameter acoustic and elastic V_P FWI were then run to 25 Hz, honouring the 15 Hz attenuation models. In Figure 2 we highlight the deeper salt body and compare the imaging from Q-compensating reverse time migrations (Q-RTMs) at 25 Hz with the corresponding elastic FWI Image. This result shows a systematic improvement in imaging quality from an acoustic Q-RTM using the acoustic FWI model (2a), to an acoustic Q-RTM using the elastic FWI model (2b), then an elastic Q-RTM using the elastic FWI model (2c), and, finally, the visco-elastic FWI Image (2d). Given that the FWI Image is derived from the velocity model, rather than a migration of the data, we see a difference in its image character, especially the larger wavenumbers, which are richer in the FWI Image. In the shallow section, we see uplift in the FWI Image compared to Q-RTM due to improved illumination provided by the full wavefield including multiples, diving waves, etc. (Zhang et al., 2020).

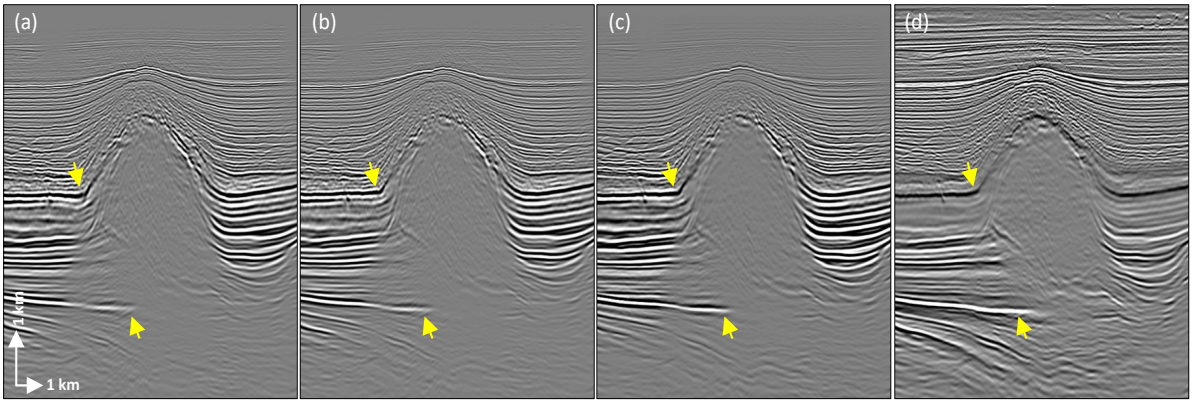

Figure 2 *Inline sections of deeper salt body: (a) 25 Hz acoustic Q-RTM using acoustic FWI model, (b) 25 Hz acoustic Q-RTM using elastic FWI model, (c) 25 Hz elastic Q-RTM using elastic FWI model, and (d) 25 Hz visco-elastic FWI Image.*

The elastic FWI was run further to a 40 Hz maximum frequency, again honouring the 15 Hz attenuation model. The comparison here is to a 40 Hz acoustic model obtained from a separate complex bespoke workflow (Refaat et al., 2021) involving aspects such as layer stripping, amongst others, to help mitigate challenges related to strong elastic parameter variations. In Figure 3 we highlight the shallower salt diapir where we see that the elastic 40 Hz model has an improved salt/sediment boundary definition and reduced halo of inversion artefacts compared with the acoustic 40 Hz model (see black arrows). In addition, the visco-elastic model shows improved velocity details in the chalk and sub-chalk layers

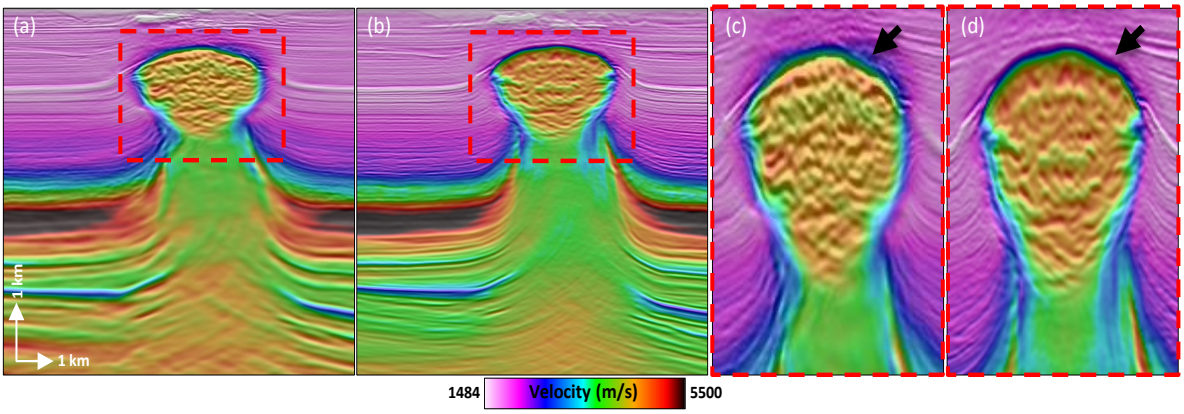

Figure 3 *Inline sections of 40 Hz V_P FWI models and corresponding FWI Image overlays: (a) visco-acoustic, and (b) visco-elastic. Panels (c) and (d) are zoom displays of the red dashed rectangles.*

In Figure 4 we compare the 40 Hz FWI Images from visco-acoustic and visco-elastic FWI. The elastic result shows improved imaging of the salt flanks and the surrounding sediments, as well as higher resolution in the chalk package and the deeper events (yellow arrows and red dashed rectangle). This highlights the improvement in event continuity, resolution, and signal-to-noise ratio (S/N) obtained from visco-elastic FWI, due to its better amplitude handling of the complex elastic wavefield.

Conclusions

We have shown a successful application of visco-elastic joint V_P and Q_P FWI driven by hydrophone data from a Central North Sea OBN survey. While the shallow Q_P anomalies derived from acoustic and elastic FWI were comparable in this case, elastic FWI generated a better P-wave velocity around the salt diapir and chalk structures. In addition, pushing visco-elastic FWI to 40 Hz provided an FWI Image with improved convergence and, therefore, better event continuity, resolution, and S/N compared with a 40 Hz visco-acoustic FWI flow. We believe the visco-elastic FWI Image provides the best result yet of this complex salt and chalk area, especially in the deep sub-salt structures. Future work can increase the maximum frequency of inversion to use more of the available bandwidth in the recorded data, as well as updating the S-wave velocity, and its quality factor, to determine its impact on P-wave imaging.

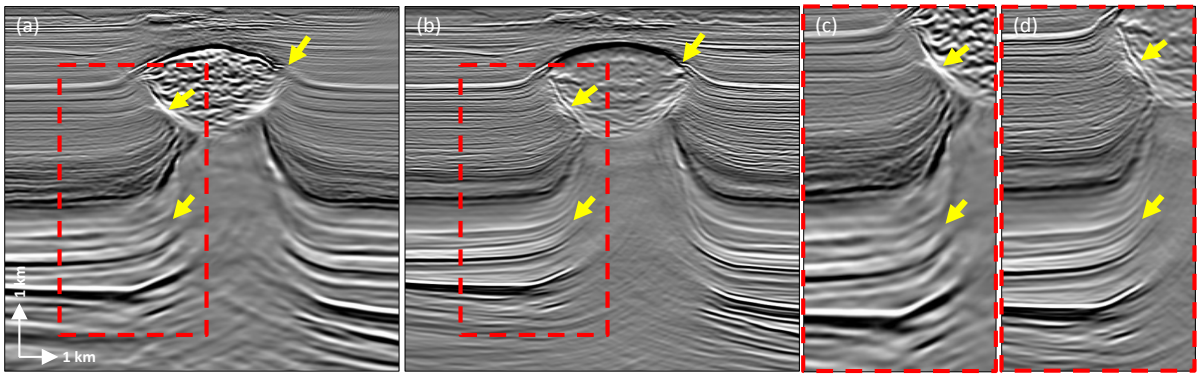

Figure 4 *Inline sections of 40 Hz FWI Images: (a) visco-acoustic, and (b) visco-elastic. Panels (c) and (d) are zoom displays of the red dashed rectangles in (a) and (b), respectively.*

Acknowledgments

We thank CGG for permission to publish, and CGG Earth Data and Magseis Fairfield ASA for permission to show the real data. We also acknowledge the work of the Cornerstone OBN team.

References

Blanch, J.O., Robertsson, J.O.A. and Symes, W.W. [1995] Modeling of a constant Q: methodology and algorithm for an efficient and optimally inexpensive viscoelastic technique. *Geophysics*, **60**, 176-184.

Carcione, J., Kosloff, D. and Kosloff, R. [1988] Wave propagation in a linear viscoelastic medium. *Geophys. J, Int.*, **95**, 597-611.

Fabien-Ouellet, G., Gloaguen, E. and Giroux, B. [2017] Time domain viscoelastic full waveform inversion. *Geophys. J. Int.*, **209**, 1718-1734.

Malinowski, M., Operto, S., and Ribodetti, A. [2011] High-resolution seismic attenuation imaging from wide-aperture onshore data by visco-acoustic frequency-domain full-waveform inversion. *Geophys. J. Int.*, **186**, 1179-1204.

Masmoudi, N., Stone, W., Ratcliffe, A., Refaat, R. and Leblanc, O. [2022] Elastic Full-Waveform Inversion for Improved Salt Model Building in the Central North Sea. *83rd EAGE Conference & Exhibition Workshop Programme*, Extended Abstracts, 1-3.

Plessix, R-E. and Krupovnickas, T. [2021] Low-frequency, long-offset elastic waveform inversion in the context of velocity model building. *The Leading Edge*, **40**(5), 342-347.

Refaat, R., Ubik, K., Sinden, J. and Holden, J. [2021] Bringing new insights to Central North Sea with OBN and FWI Imaging. *82nd EAGE Conference & Exhibition*, Extended Abstracts, 1-5.

Robertsson, J.O.A., Blanch, J.O. and Symes, W.W. [1994] Viscoelastic finite-difference modeling. *Geophysics*, **59**, 1444-1456.

Stopin, A., Plessix, R.-E., Kuehl, H., Goh, V. and Overgaag, K. [2016] Application of Visco-acoustic Full Waveform Inversion for Gas Cloud Imaging and Velocity Model Building. *78th EAGE Conference & Exhibition*, Extended Abstracts, Tu STZ0 12.

Wang, H., Burtz, O., Routh, P., Wang, D., Violet, J., Lu, R., and Lazaratos, P. [2021] Anisotropic 3D elastic full-wavefield inversion to directly estimate elastic properties and its role in interpretation. *The Leading Edge*, **40**(5), 277-286.

Xiao, B., Ratcliffe, A., Latter, T., Xie, Y. and Wang, M. [2018] Inverting for near-surface absorption with full-waveform inversion: a case study from the North Viking Graben in the northern North Sea. *80th EAGE Conference & Exhibition*, Extended Abstracts, Tu A12 03.

Wu, Z., Wei, Z., Zhang, Z., Mei, J., Huang, R. and Wang, P. [2022] Elastic FWI for large impedance contrast. *2nd International Meeting for Applied Geoscience & Energy, SEG/AAPG*, Expanded Abstracts, 3686–3690.

Yang, P., Brossier, R., Metivier, L. and Virieux, J. [2016] A review on the systematic formulation of 3-D multiparameter full waveform inversion in viscoelastic medium. *Geophys. J. Int.*, **207**, 129-149.

Zhang, Z., Wu, Z., Wei, Z., Mei, J., Huang, R. and Wang, P. [2020] FWI Imaging: Full-wavefield imaging through full-waveform inversion. *90th Annual International Meeting, SEG*, Expanded Abstracts, 656-660.